Insights into mine tailings mechanical response under plane-strain compression and stress path testing

Cody Arnold[a], Jorge Macedo[a]

[a]*School of Civil and Environmental Engineering, Georgia Institute of Technology, Atlanta, GA, United States*

Abstract

Mine tailings storage facilities (TSFs) are commonly analyzed under plane-strain assumptions, yet experimental data on tailings behavior under this condition are absent from the literature. This study uses a plane-strain apparatus capable of measuring intermediate stress to investigate drained and undrained compression and constant shear drained (CSD) responses of a non-plastic mine tailing. The critical state line (CSL) from plane-strain testing is shown to be identical to that from triaxial testing on the same material, supporting CSL uniqueness in e–p' space. The critical stress ratio under plane strain falls within Mohr-Coulomb and Matsuoka-Nakai bounds, consistent with prior findings on sands. Intermediate stress ratios (b) range from 0.25–0.30 under drained loading and 0.30–0.48 under undrained loading. Under CSD loading, all specimens exhibit Type-I instability at the transition from volumetric expansion to contraction, with onset near the lower bound of the expected critical state stress ratio range. The intermediate stress development is stress-path dependent, producing a distinct CSD response relative to compression loading. These findings represent the first known experimental investigation of mine tailings under zero-lateral strain conditions (plane-strain) that tracks intermediate stresses and provides a basis for improving TSF stability assessments.

keywords: Plane-Strain, Mine Tailings, Static Liquefaction, Intermediate Stress

1. Introduction

Plane strain is a deformation condition in which strain in one principal direction, typically the intermediate direction, is zero ($\varepsilon_2 = 0$), while the corresponding stress (σ_2) remains

nonzero. Deformation is therefore confined to a two-dimensional plane, and the principal stresses σ_1, σ_2, and σ_3 evolve under this constraint. Many geotechnical systems, including dams, embankments, excavations, and retaining walls, are often evaluated under plain strain, making it highly relevant in geotechnical engineering (Rowe, 1969).

Critical State Soil Mechanics (CSSM) (Roscoe et al., 1958; Schofield and Wroth, 1968) provides a framework for interpreting soil behavior under different loading conditions, including plane strain. A key element of CSSM is the existence of a critical state surface, typically projected as lines in the void ratio–mean effective stress (e–p') and mean effective stress–deviatoric stress (p'–q) spaces, referred to as critical state lines (CSLs). The role of loading mode, relevant for plane-strain deformation, is characterized by the intermediate stress ratio, b value ($\frac{\sigma_2 - \sigma_3}{\sigma_1 - \sigma_3}$), or equivalently by the Lode angle, θ ($\cos^{-1}\left(\frac{1-2b}{\sqrt{3}}\right)$). b values of 0 and 1 correspond to triaxial compression and extension, respectively. Under plane strain, b lies between these limits and evolves during loading. There is general agreement that the CSL in p'–q space depends on the Lode angle (Jefferies and Been, 2016). However, in the e–p' space, there are contrasting findings. Some studies report distinct CSLs under varying loading modes (Riemer and Seed, 1997; Wagner et al., 2023; Yoshimine et al., 1998), while others observe a unique CSL independent of loading mode (Becker et al., 2022; Been et al., 1991; Fanni et al., 2024; Salvatore et al., 2017; Schnaid et al., 2013). When differences are reported, they are typically attributed either to Lode angle dependence (Wanatowski and Chu, 2007) or to a non-unique CSL (Riemer and Seed, 1997).

Experimental investigations under plane strain have focused primarily on sands. Only a few studies have measured intermediate stresses, and to our knowledge, only Wanatowski and Chu (2007) explicitly incorporated such measurements to support CSL characterization. Measurement of the intermediate stress is key for robust CSL interpretation because it defines the development of stresses under plane-strain conditions. Table 1 summarizes previous efforts that implement plane-strain testing, highlighting those that measure inter-

mediate stresses. None of these studies considered mine tailings. The most comprehensive investigation to date is the series of studies by Wanatowski (2005); Wanatowski and Chu (2006, 2007), who tested Changi sand under both triaxial and plane strain and reported developing b values between 0.20 and 0.40 under plane strain. They identified distinct CSL in e–p' space, with plane-strain yielding a higher intercept (Γ) and similar slope (λ) relative to triaxial condition. In contrast, Finno et al. (1996) reported both increased Γ and reduced λ in plane strain, while Finno and Rechenmacher (2003) observed density-dependent variation in Γ. These contrasting findings underscore the lack of consensus on CSL characterization under plane-strain.

Most plane-strain studies have considered compression loading, although other loading modes are also relevant. Constant shear drained (CSD) loading has been, in particular, associated with major dam failures (Arroyo and Gens, 2022; Been et al., 1987; Morgenstern et al., 2019, 2016; Olson et al., 2000). In laboratory testing, CSD is implemented by decreasing p' at constant q. Several recent studies have examined CSD behavior under triaxial conditions (e.g., Fotovvat et al., 2022; Reid et al., 2024; Riveros and Sadrekarimi, 2021; Vergaray and Macedo, 2024). However, to our knowledge, Wanatowski et al. (2010) remains the only experimental investigation of CSD under imposed plane-strain conditions explicitly measuring intermediate stresses.

For mine tailings, investigations of loading-mode effects remain limited. Wagner et al. (2023) reported distinct CSLs in e–p' space under triaxial compression and extension, whereas Fanni et al. (2024) observed a unique CSL from hollow-cylinder and triaxial tests at fixed b values (0, 0.5, and 1). In those experiments, b was imposed and remained constant during shearing, unlike plane-strain loading where it develops. Velten et al. (2025) interpreted undrained simple shear tests on copper tailings as representative of plane-strain conditions and derived a CSL. However, intermediate stresses were not reported, and the plane-strain assumption was not fully substantiated, since constant height and undrained conditions do

Table 1: Plane-strain devices used in publications adapted from Wanatowski (2005) and expanded with more recent studies.

Location	Specimen Size (WxLxH) (mm)	out-of-plane Stress	Reference(s)
Imperial College, London, UK	51x406x102	Yes	Bishop (1958) Cornforth (1961) Cornforth (1964)
Technical University of Karlsruhe, Germany	200x1000x600	Yes	Leussink and Wittke (1964)
University of California, Berkeley, USA	28x71x61 28x71x71	No	Duncan and Seed (1966) Lee (1970)
University of Cambridge, UK	70-130x 70-130x50	Yes	Hambly (1969) Hambly and Roscoe (1969) Hambly (1972)
University of British Columbia, Canada	25x100x57	Yes	Campanella and Vaid (1973)
University College, London, UK	100x100x100	Yes	Arthur et al. (1985) Yasin et al. (1999)
University of Karlsruhe, Germany	45-133x 45-133x50	Yes	Topolnicki et al. (1990)
University of Minnesota, USA	40x80x140	No	Drescher et al. (1990)
Northwestern University, USA	40x80x140	Yes	Finno et al. (1996) Finno et al. (1997)
Laboratoire 3S-IMG, Grenoble, France	35x90-135x 75-350	No	Desrues et al. (1985) Desrues et al. (1996) Desrues and Viggiani (2004)
University of Tokyo, Japan	40x80x105 80x160x140	Yes	Tatsuoka et al. (1986) Tatsuoka et al. (1994) Yasin et al. (1999)
Louisiana State University, USA	60x120x180	No	Alshibli et al. (2004)
Guangzhou University, China	60x80x160	No	Wu et al. (2020)
Nanyang Technological University, Singapore	60x60x120	Yes	Wanatowski (2005) Wanatowski and Chu (2006) Wanatowski and Chu (2007) Wanatowski et al. (2008) Wanatowski et al. (2010) Wanatowski and Chu (2012) Wang et al. (2024)
Georgia Institute of Technology, USA	40x80x140	Yes	Evans (2005) Frost and Evans (2009) Frost et al. (2012)
Georgia Institute of Technology, USA	40x100x120	Yes	Arnold (2025)

not inherently impose zero out-of-plane strain without a physical lateral constraint. The scarcity of plane-strain investigations on tailings is significant because tailings often exhibit distinct behavior compared to natural soils, e.g., higher compressibility and distinct stiffness–strength scaling (Jefferies and Been, 2016; Macedo and Vergaray, 2021), while stability analyses of tailings storage facilities commonly assume plane-strain conditions.

Given the limited efforts investigating mine tailings under plane-strain loading, particularly those measuring the intermediate stress required for robust CSL characterization, further work is needed to advance understanding of tailings response under plane strain within the CSSM framework. This study contributes in that direction by presenting drained and undrained compression and CSD tests performed using a plane-strain apparatus capable of measuring intermediate stress. The objectives are to gain insights on the overall mechanical response under plane-strain conditions, evaluate whether the CSL under plane strain differs from that obtained in triaxial loading, and to examine the onset of instability under plane-strain loading paths.

The next section describes the plane-strain apparatus, testing procedures, and the tested mine tailings. We then present the experimental results, followed by a discussion of CSL characterization and instability under both undrained compression and CSD loading.

2. Experimental Program

2.1. Plane-Strain Apparatus Configuration

Figure 1 presents the main components of the plane-strain apparatus, including the load frame, external and internal load cells, a linear variable differential transformer (LVDT) for axial displacement measurement, a pore pressure transducer, two syringe pumps for volume and pressure control, and lateral pressure sensors. The system accommodates specimens with dimensions of 120 mm $\times$ 100 mm $\times$ 40 mm. A detailed description of the apparatus and its implementation is provided by Arnold (2025); only the key features relevant to this study are summarized herein.

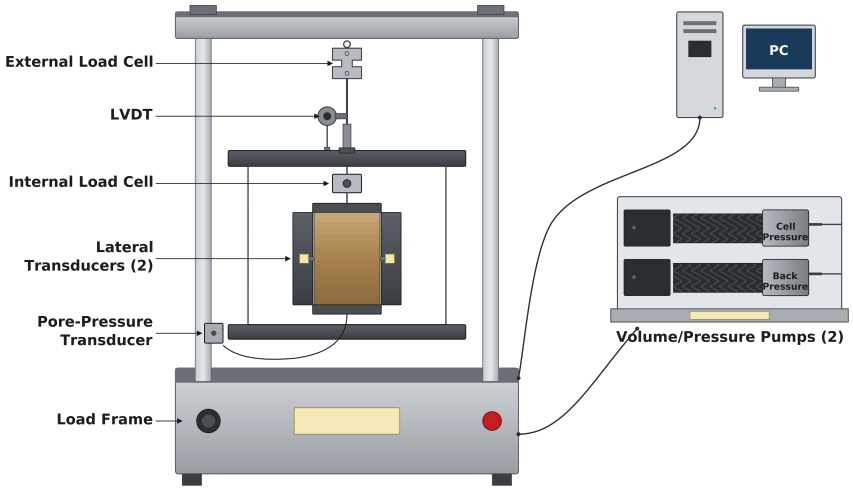

Figure 1: Overview of plane-strain apparatus components.

The LVDT is mounted at the top of the cell, and an internal submersible load cell is positioned directly above the specimen. An integrated microprocessor-based data acquisition system enables real-time monitoring and closed-loop control of stress paths. This capability is essential for tests such as CSD, which require continuous control of stresses as the specimen approaches instability. The load frame interfaces with a computer that provides real-time monitoring and direct control of testing commands.

A key feature of the apparatus is the direct measurement of intermediate stress. Two miniature earth pressure sensors from Kyowa Electronic Instruments are embedded at mid-height within the lateral restraining plates to achieve this. Their central placement follows the recommendations of Frost and Yang (2003), who showed that the middle region of specimens is less affected by top and bottom boundary effects. Figure 2 illustrates the final design of the restraining plate and sensor configuration, including (a) the front view, (b) a schematic side profile, and (c) the configuration with the specimen installed.

2.2. Testing Material

The material tested in this study is a non-plastic mine tailing classified as a well-graded silty sand based on the particle size distribution shown in Figure 3. The mineralogical

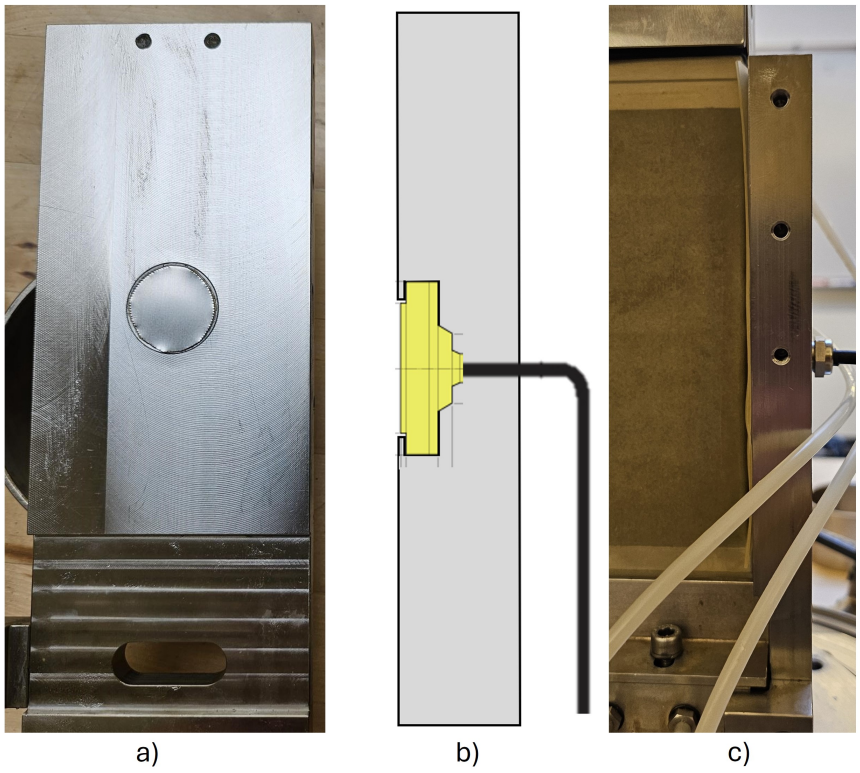

Figure 2: The intermediate pressure sensor and restraining plate design at a) the front face, b) schematic of the side profile, and c) the side of the plate highlighting the location at mid-height of the specimen.

composition is predominantly quartz (78%), with chlorite comprising approximately 20% as determined by X-ray diffraction with mineral quantification Rietveld (1969). Scanning electron microscope (SEM) images indicate predominantly subangular, rough particles. Finer particles are embedded within the coarse matrix and adhere to larger grains, resulting in a mixed coarse–fine contact structure rather than a purely sand-like skeleton (Figure 3). Table 2 summarizes the index and physical properties of the tailings. Vergaray and Macedo (2024) performed triaxial testing on the same material. Their results will be used to compare against the interpretation of the plane strain tests conducted in this study and are discussed in later sections.

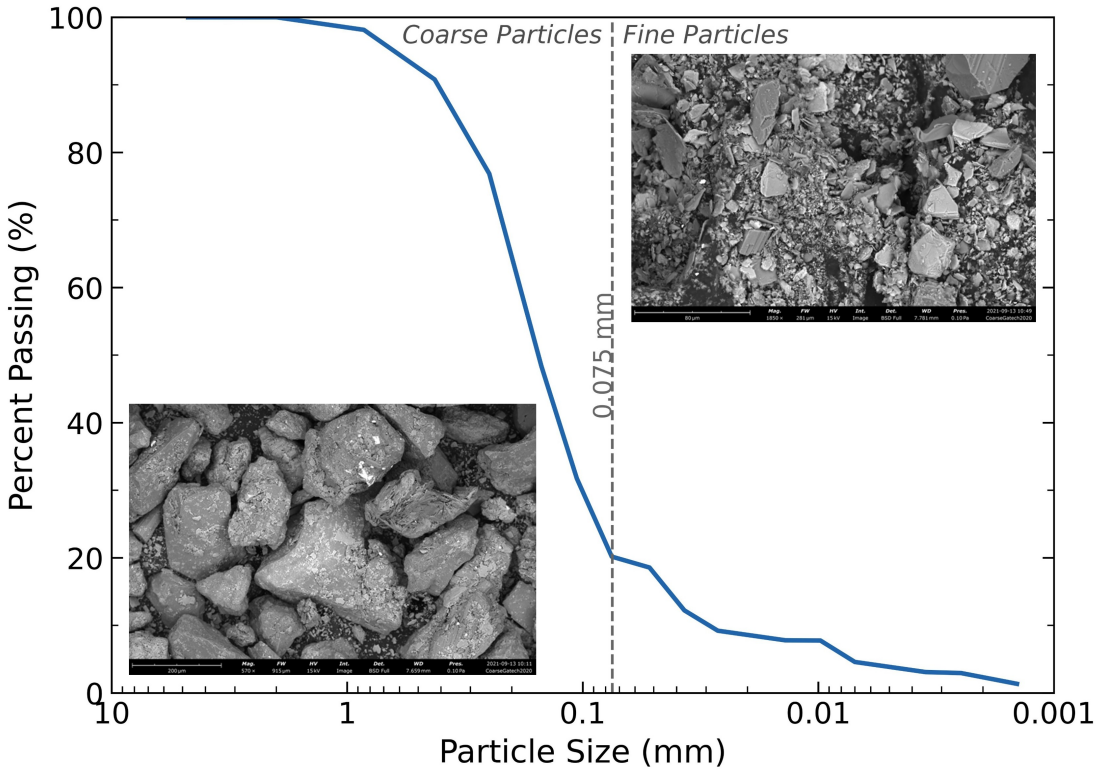

Figure 3: Particle size gradation of tested tailing with SEM showing coarse particles (x570 magnification) and fine particles (x1850 magnification).

Table 2: Material properties, critical state parameters, and mineralogy.

Material Properties		Critical State Parameters		Mineralogy	
Plasticity Index (PI)	0	λ	0.034	Quartz (%)	78
Fine Contents (FC)	20%	Γ	0.75	Chlorite (%)	20
Specific Gravity (G_s)	2.80	M_{tc}	1.32	Other (%)	2
Coefficient of Uniformity (C_u)	6				

2.3. Experimental Procedure

Loose specimens were prepared using the under-compaction technique (Ladd, 1978) to promote uniformity. This method is widely adopted for critical state testing of mine tailings (Jefferies and Been, 2016; Reid et al., 2020). After molding, the restraining plates were positioned on either side of the specimen and secured to the base platen using two retaining screws per side. The screws were tightened alternately to minimize stress bias. Additional lateral support bars were installed across the top of the plates to enhance system rigidity.

An end-of-test freezing (EOTF) procedure was implemented to determine void ratio (Figure A.1), as it reduces measurement error in critical state line testing (Jefferies and Been, 2016; Reid et al., 2020). In addition, a procedure was adopted to promote plane-strain conditions prior to shearing. Based on linear elasticity and Hooke's law (Equation 1), the plane-strain condition ($\varepsilon_2 = 0$) yields:

$$\epsilon_2 = \frac{1}{E}\left(\sigma_2 - \nu(\sigma_1 + \sigma_3)\right) \tag{1}$$

$$\sigma_2 = \nu(\sigma_1 + \sigma_3) \tag{2}$$

Assuming a Poisson's ratio $\nu = 0.3$ and recognizing that σ_2 is initially close to σ_3 (applied cell pressure), the following relation is obtained:

$$\sigma_1 = 2.33\sigma_3 \tag{3}$$

Accordingly, to promote zero lateral strain prior to shearing, the deviatoric stress was maintained at $q = \sigma_1 - \sigma_3 \approx 1.33\sigma_3$.

Figure 4 illustrates the evolution of displacement, principal stresses, and pore volume during flushing and consolidation. During flushing (Figure 4a), the intermediate stress initially differs from the applied lateral stress because the specimen is partially unsaturated. As flushing progresses, vertical displacement stabilizes at approximately 10,000 s, indicating completion of most volume change due to flushing. Concurrently, intermediate stress readings stabilize and increase toward the applied lateral stress, reflecting adequate specimen-to-plate contact. This stage coincides with the progressive removal of entrapped air, after which no further air is observed exiting the top drainage lines. Figure 4b shows the sample response during consolidation. In this case, the consolidation was conducted in two stages. Each stage involved increases in vertical and lateral stresses accompanied by vertical displacement that rapidly stabilized. Intermediate stress readings increased accordingly and ultimately matched the applied lateral stress, confirming proper sensor response and lateral confinement. These responses were achieved following iterative refinement of the apparatus design described in Arnold (2025).

A total of 14 tests were conducted (Table A.1), including plane-strain compression and CSD, and triaxial extension tests. Compression tests (drained and undrained) were performed at a strain rate of 2% per hour, and CSD tests employed a stress reduction rate of 1 kPa per minute.

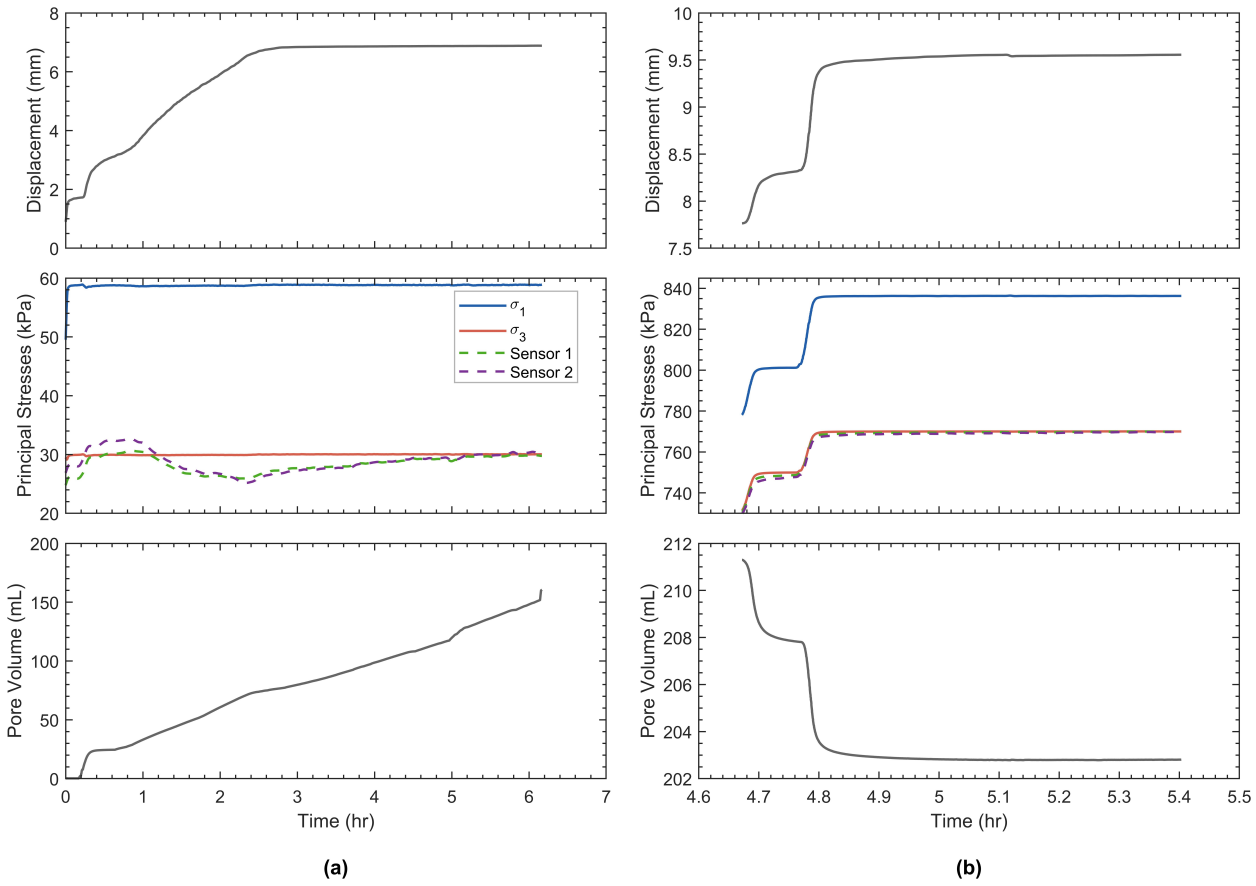

Figure 4: Time series of displacement, principal stresses, and pore volume during (a) flushing and (b) consolidation stages during plane-strain testing.

3. Insights from Plane-Strain Testing

Vergaray and Macedo (2024) conducted triaxial tests on the same tailings. Selected representative results are summarized to provide context for the plane-strain responses.Figures 5a and 5b show representative triaxial responses for loose initial states, which are of primary interest for this study. Under undrained loading, the specimens exhibit strain softening, with q decreasing after peak and excess pore pressures increasing during shearing, behavior commonly associated with static liquefaction (Macedo and Vergaray, 2021). Under drained loading, q increases monotonically, and positive volumetric strains (contraction) develop. These responses are consistent with the initially loose state of the material.

Figures 5c and 5d present the corresponding stress paths in the e–p' and p'–q spaces used to define the CSL. The resulting $\lambda = 0.034$ indicates relatively low compressibility, within the typical range for natural sands and silts (0.02–0.04; Jefferies and Been (2016)). In contrast, $M_{tc} = 1.32$ exceeds values commonly reported for sands (Jefferies and Been, 2016), likely reflecting the angular and rough particle morphology of the tested tailings (Figure 3).

Figure 6 compares triaxial and plane strain responses for comparable loose states under undrained loading. In both cases, q reaches a peak followed by softening (Figure 6a,c). Under triaxial loading, the intermediate stress equals the minor stress (b=0), whereas under plane strain, the intermediate stress is not fixed and instead develops during loading. The plane-strain test reaches a b value of about 0.48 (Figure 6b). The triaxial p'–q paths converge to an $M_{tc} = 1.32$ whereas in plane strain M varies with the associated b value development (Figure 6c), with the shaded region representing the plausible M range from our testing (discussed later). Instability is identified at the peak of p'–q stress paths (Bokkisa and Macedo, 2025). In e–p' space (Figure 6e), both loading modes follow contractive paths characterized by decreasing p' at nearly constant e prior to instability, accompanied by excess pore pressure generation (Figure 6f).

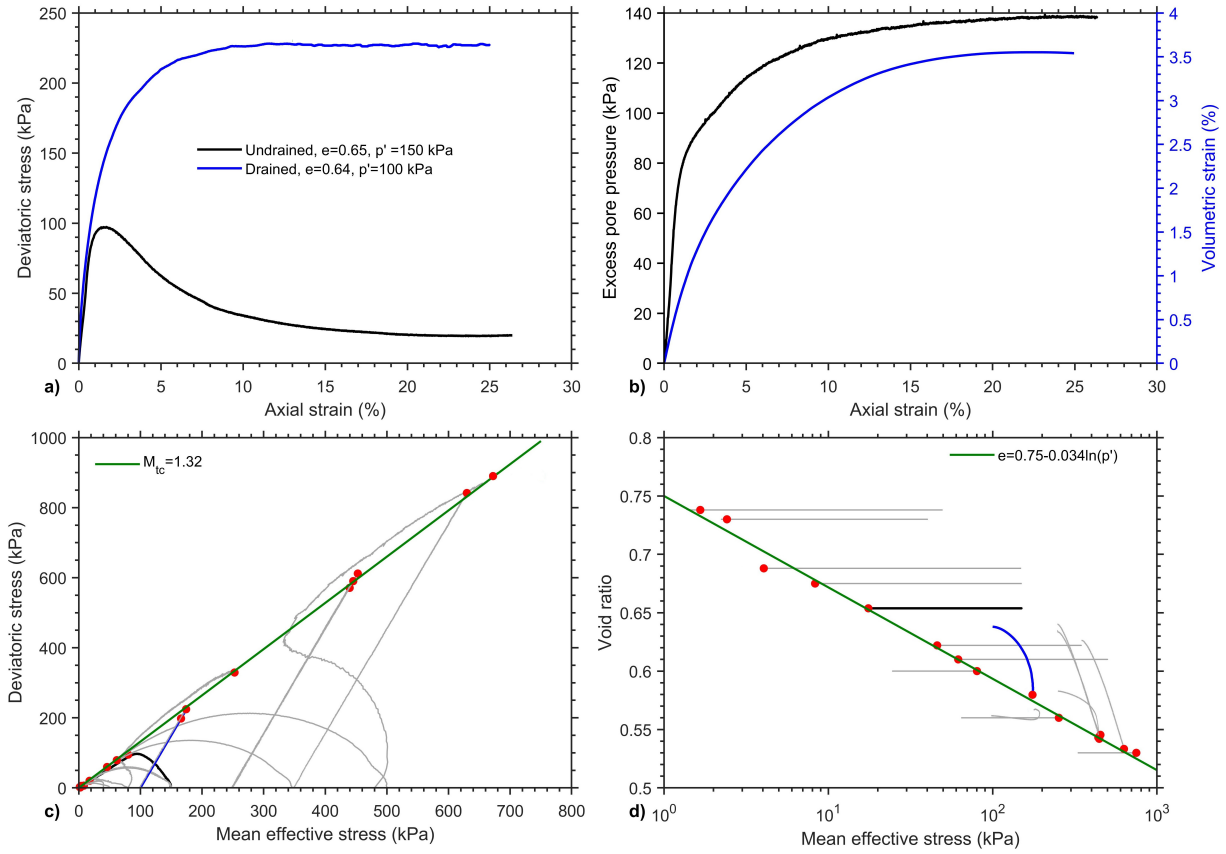

Figure 5: Representative drained and undrained responses for the tested tailing under triaxial conditions. (a) Deviatoric stress q versus axial strain for the undrained (black; $e = 0.65$, $p'_0 = 150$ kPa) and drained (blue; $e = 0.64$, $p'_0 = 100$ kPa) tests. (b) Excess pore pressure for the undrained test (left axis) and volumetric strain for the drained test (right axis) versus axial strain. (c) Stress paths in the p'–q plane, tests on panels (a) and (b) are highlighted. (d) Evolution in the p'–e, red markers indicate interpreted critical state conditions. Tests conducted by Vergaray and Macedo (2024).

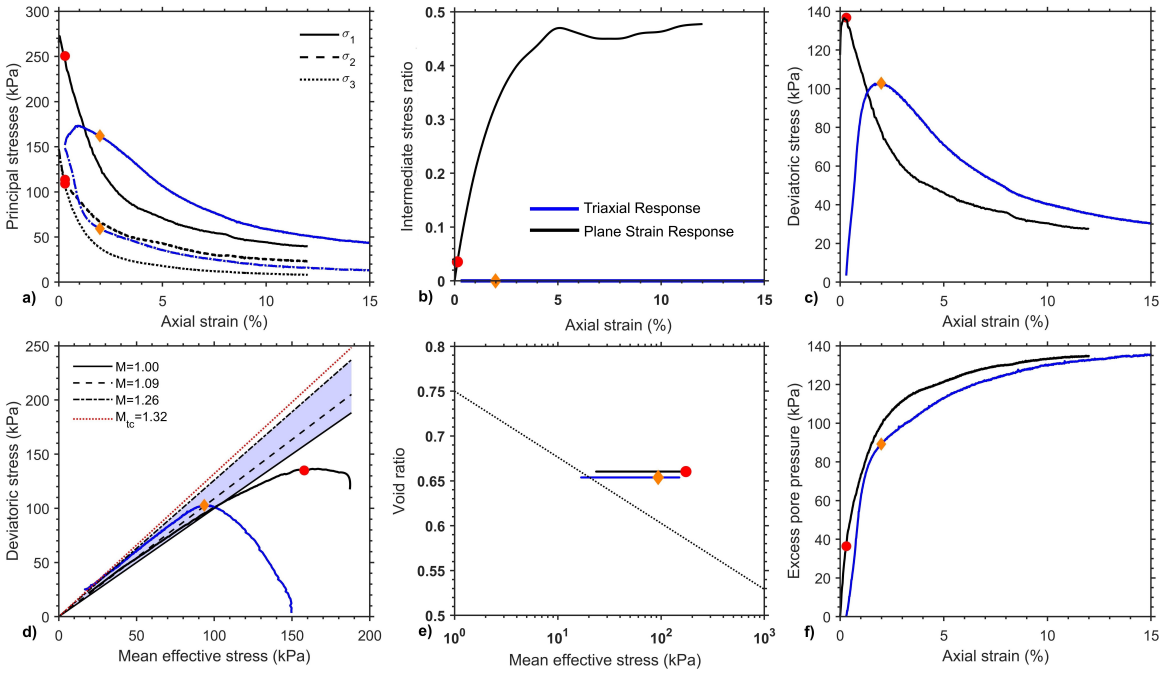

Figure 6: Undrained plane-strain (PS6) and triaxial (TX5) responses for comparable initial conditions; triaxial test selected from Vergaray and Macedo (2024).

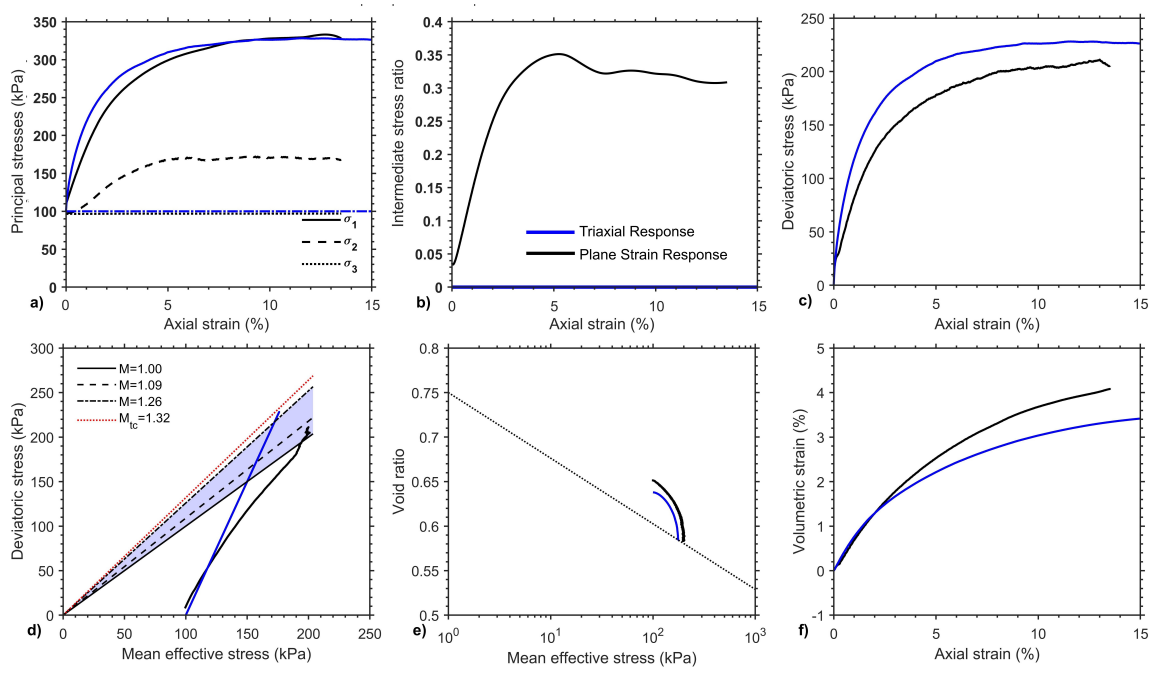

Figure 7: Drained plane-strain (PS8) and triaxial (TX7) responses for comparable initial conditions; triaxial test selected from Vergaray and Macedo (2024).

Figure 7 compares drained responses under triaxial and plane-strain loading. The evolution of q is similar in both cases (Figure 7c); the principal stress components differ as expected in plane strain, while in triaxial loading, $\sigma_2 = \sigma_3$ (Figure 7a). The plane strain test reaches a b value of about 0.32 (Figure 7b). Again, $M_{tc} = 1.32$ in triaxial, compared with the variable M in plane-strain loading, which is lower (Figure 7d). In e–p' space (Figure 7e), both loading modes exhibit contractive behavior consistent with the loose initial state, which is also observed in the evolution of volumetric strains (Figure 7f).

Figure 8 presents the responses for all plane-strain tests. The q–axial strain responses confirm contractive behavior (Figure 8a). Figure 8b shows that at large strains, b typically ranges between 0.25 and 0.30 in drained loading and between 0.30 and 0.48 in undrained loading. This indicates stress-path-dependent evolution of intermediate stress, consistent with Wanatowski and Chu (2007), who also observed larger b in plane strain compression undrained loading. The p'–q paths vary from $M \approx 1to1.14$ (Figure 8c). A range of plausible M under plane strain that will be discussed later is also shown. Figure 8d shows that the e–p' stress paths are contractive in both drained and undrained tests, with p' decreasing under constant e in undrained loading and e decreasing with p increasing under drained loading.

Figure 9 examines the relationship between M and b using the Mohr–Coulomb and Matsuoka–Nakai criteria. Changi Sand reported by Wanatowski and Chu (2007) show $M_{tc} = 1.35$; accordingly, the curves are normalized to this value at $b = 0$. The tailings tested in this study exhibit $M_{tc} = 1.32$ at $b = 0$. Jefferies and Shuttle (2002) suggested that the average of the Mohr-Coulomb and Matsuoka-Nakai criteria reasonably represents the M–b relationship observed by Cornforth (1961) for Brasted sand. A similar trend is observed in the data of Wanatowski and Chu (2007), although some points approach or exceed the Matsuoka-Nakai bound. The results from the present study also fall between the Mohr-Coulomb and Matsuoka-Nakai criteria; however, most data cluster near the average trend.

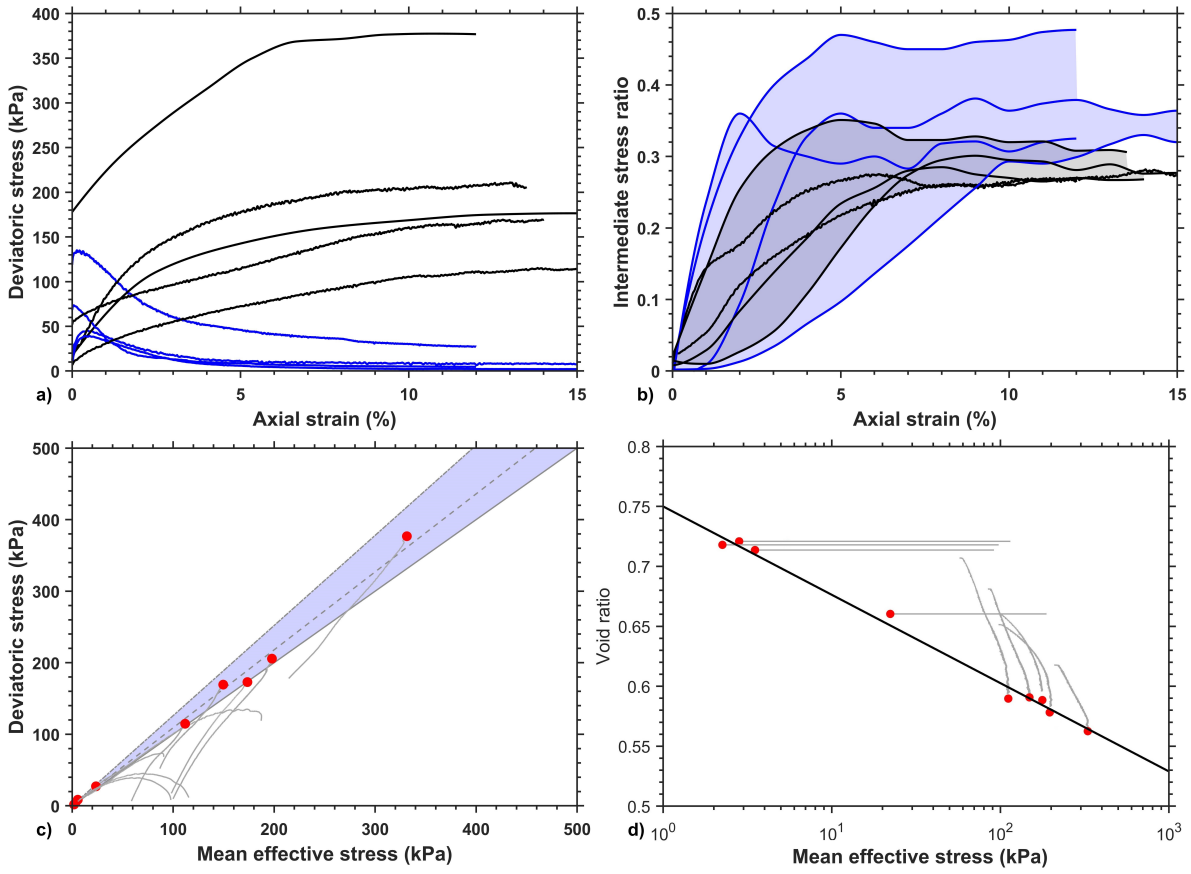

Figure 8: Plane-strain test responses: (a) q versus axial strain; (b) b value versus axial strain; (c) p'–q stress paths with interpreted M range; and (d) e–p' responses with interpreted critical state line. Red markers indicate interpreted critical state points.

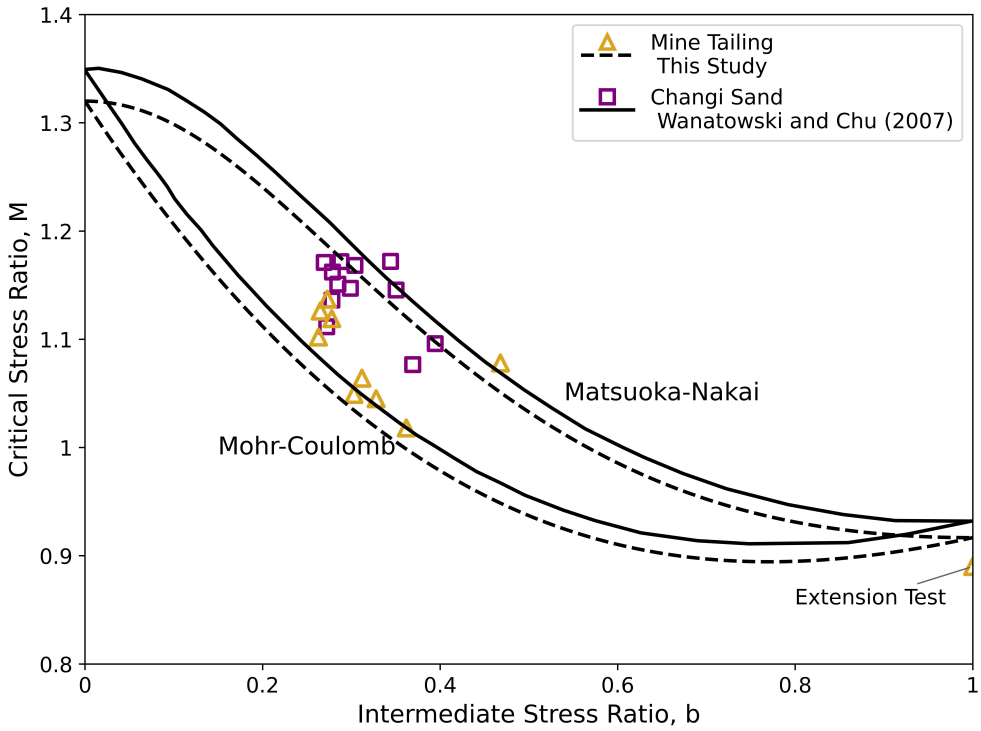

Figure 9: Reliance of critical stress ratio (M) on b value for the considered mine tailings with data on a clean sand from Wanatowski and Chu (2007).

Based on the estimated b range and the bounding criteria, M values between 1.00 and 1.26 can be inferred. However, the maximum M observed from our tests was about 1.14.

3.1. Critical State Interpretation

Figure 8c and Figure 8d show the interpreted plane-strain CSL in q–p' and e–p' spaces. In the e–p' space, the criteria by Torres-Cruz and Santamarina (2019) were adopted for interpretations. The q–p' plot includes the estimated M range and an averaged value $M = 1.09$. The resulting ratio $M/M_{tc} \approx 0.83$ falls within the range reported by Cornforth (1961, 1964) and Wanatowski and Chu (2006).

In e–p' space, the plane-strain CSL yields $\Gamma = 0.75$ and $\lambda = 0.032$. Compared with the triaxial interpretation, the intercept is identical, and the slope differs by only 0.002. Within experimental uncertainty, this supports a unique CSL for triaxial and plane strain loading for this tailing. For reference, the round-robin CSL program of Reid et al. (2020) reported deviations in void ratio of up to 0.04 across laboratories testing the same material. The present result, indicating the same CSL in e–p' space, contrasts with Wanatowski and Chu (2007), the only previous study, to our knowledge, that directly measured intermediate stresses to define the CSL under plane-strain conditions. Wanatowski and Chu (2007) reported parallel CSLs for plane-strain and triaxial loading, differing by 0.05 in void ratio.

4. Drained Instability

Figure 10 compares representative responses from triaxial and plane-strain CSD loading. The onset of instability is highlighted in both cases based on Hill's criterion (Hill, 1958).

Figure 10a shows the evolution of the principal stresses. During stress relief in plane strain, all three principal stresses decrease at different rates because σ_2 is not directly controlled. As instability begins, the intermediate stress in plane strain starts to increase more rapidly, while in triaxial loading the decrease in stresses continues at a relatively steady rate. At this stage, the volumetric strain reverses its trend from increase to decrease in

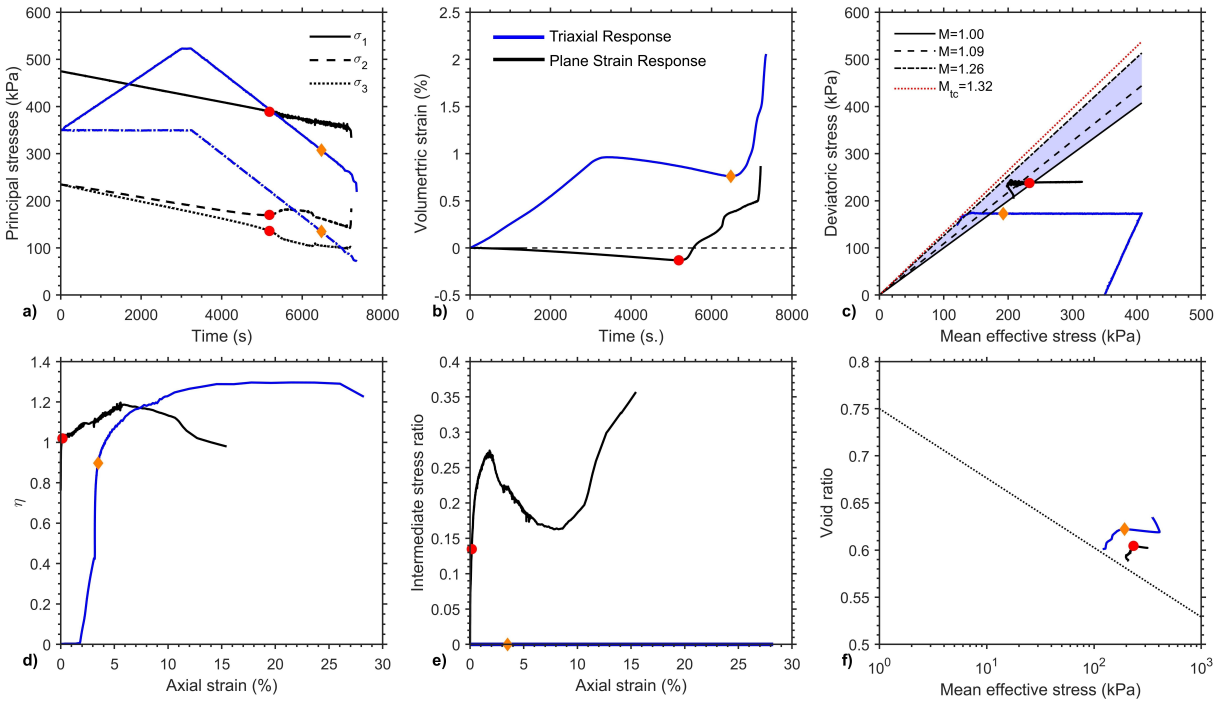

Figure 10: Comparison of selected CSD tests from this study (PS12) and Vergaray and Macedo (2024) (TX17); (a) Principal stresses versus time, (b) Volumetric strain versus time, (c) Stress paths in the p'–q plane, (d) Stress ratio $\eta = q/p'$ versus axial strain, (e) b value versus axial strain, and (f) Void ratio versus p'. Markers denote the selected instability points for each dataset.

both loading modes (Figure 10b). This form of response corresponds to Type I instability for loose materials, as described by Vergaray and Macedo (2024) and Alipour and Lashkari (2018) for triaxial loading. The same mechanism is observed here under plane-strain conditions. Figure 10c shows the p'–q stress paths and highlights the instability point. In plane strain, instability occurs near the lower bound of the expected range of M. This contrasts with the triaxial response, where instability develops further from the corresponding M_{tc}. Figure 10d shows the evolution of the stress ratio η. In both loading modes, instability occurs while η is increasing. Notably, instability develops at small axial strains (less than approximately 0.5% after stress-relief) in both cases. Figure 10e shows the evolution of the b value. In triaxial loading, b remains fixed at zero, whereas in plane strain it evolves during shearing, with instability occurring during the initial b value development. Figure 10f shows the e–p' stress paths. In both loading modes, e increases during stress relief until instability occurs, after which e decreases, consistent with Type I instability. A slight difference is that the pre-instability increase in e is somewhat less pronounced in plane strain, which may be influenced by the more positive initial state of the triaxial specimen.

Figure 11 presents the responses of three CSD tests under plane-strain conditions. In these tests, stress relief was applied immediately after consolidation, as the K_0 consolidation resulted in a relatively high stress ratio. The p'–q stress paths (Figure 11a) follow the same pattern discussed above, with instability reached near the lower bound of the expected plane-strain M range. Unlike Wanatowski et al. (2010), whose apparatus encountered difficulties maintaining stress control near instability, the device used in this study allowed observation beyond instability onset. The stress ratio $\eta = q/p'$ continued to increase until the constant-q condition could no longer be maintained. This occurred within the expected M range discussed before, but at higher M values than those observed in plane-strain compression loading. These results indicate that intermediate stress development depends on the imposed stress path, consistent with the suggestions of Wanatowski et al. (2010). This observation

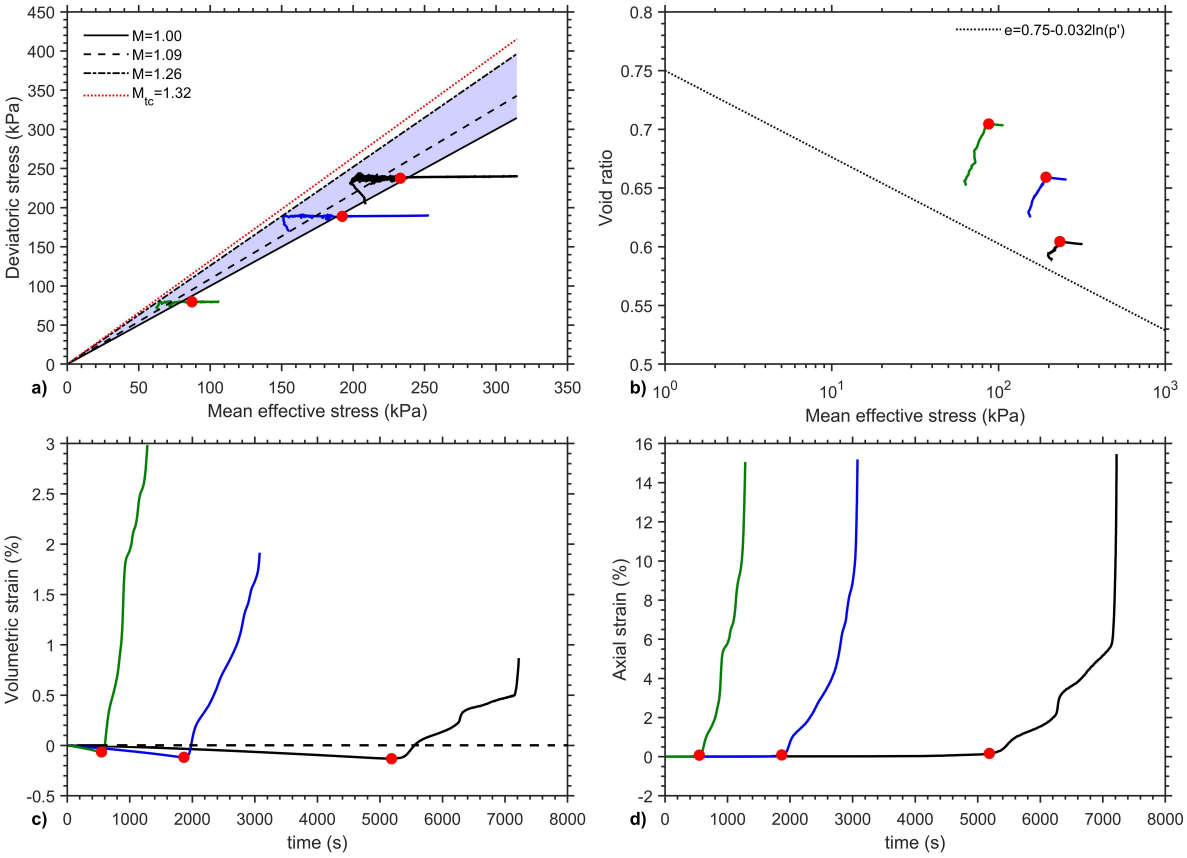

Figure 11: Response of CSD load path testing under 106 kPa (green), 252 kPa (blue), and 317 kPa (black) of confinement. (a) Stress paths in the p'–q plane.(b) Void ratio versus p'. (c) Volumetric strain versus time. (d) Axial strain versus time. Red dots denote the instability points identified as the maximum void ratio ($e_{\max}$) for each test and projected consistently across all subplots.

on stress path dependence also aligns with the different b value ranges previously discussed for drained and undrained plane-strain compression tests.

In e–p' space (Figure 11b), all responses are consistent with Type I instability. At instability, each test shows a reversal of volumetric strain from increase to decrease (Figure 11c). This behavior is consistent with the mechanism proposed by Vergaray and Macedo (2024) and Bokkisa and Macedo (2025), in which instability results from the interaction between elastic and plastic volumetric components. During initial stress relief (decrease in p'), volume increases because elasticity dominates. As η continues to increase, plastic volumetric strains develop due to dilatancy. Eventually, plastic contraction exceeds elastic expansion, leading to a net volume decrease. Instability occurs at the transition point, after which plastic strains dominate. Following instability, axial strains increase rapidly as η continues to rise (Figure 11d).

The response of the loose specimens resembles that reported by Wanatowski et al. (2010) for test IND01. However, their device was not able to maintain constant q near instability, and volumetric strain was shown for only one loose test. Consequently, the volumetric behavior of their loose specimens remains inconclusive. The three plane-strain responses presented here therefore provide additional insight into the response under plane-strain CSD loading.

5. Discussion

The CSL interpretation (Figures 6, 7, 8, and 9) and CSD stress paths (Figures 10 and 11) are notable in the context of existing literature. The debate over CSL uniqueness in the e–p' space under enforced plane-strain conditions with evolving intermediate stress is largely based on testing using the same device and only Changi sand with the same gradation (Wanatowski, 2005; Wanatowski and Chu, 2007; Wanatowski et al., 2008). Furthermore, Wanatowski et al. (2010) remains the only study addressing drained instability under plane-

strain conditions. The present results differ from those reported by Wanatowski and Chu (2006, 2007) in some aspects; hence, it is relevant to discuss the potential cause(s).

Although this study focuses on mine tailings and Wanatowski and Chu (2007) examined clean sand, differences in soil type alone are unlikely to explain the discrepancies. A key distinction lies in the estimation of void ratio, which is known to influence CSL interpretation (Jefferies and Been, 2016; Reid et al., 2020; Sladen and Handford, 1987). Common methods based on specimen dimensions are prone to error due to geometric irregularities and measurement limitations. Wanatowski (2005) employed the method of Verdugo and Ishihara (1996), based on end-of-test gravimetric water content. While post-shearing void ratio estimation is often preferred, it is not recommended for CSL determination in tailings engineering (Jefferies and Been, 2016; Reid et al., 2020). In the Reid et al. (2020) round-robin program focused on evaluating CSLs for a mine tailings, some participants used the Verdugo and Ishihara (1996) method, and in fact, one of the entries using the method resulted in one of the largest deviations. In contrast, participants incorporating end-of-test freezing (EOTF) yielded more consistent results. These observations suggest that void ratio measurement may have contributed to the different CSLs for triaxial and plane strain conditions reported by Wanatowski and Chu (2007).

To further assess CSL uniqueness in e–p' space, two additional undrained triaxial extension tests were conducted (Figure 12), comparing against the previously discussed plane strain test and a selected triaxial compression test. For comparable initial states, the extension response is more contractive than triaxial compression, consistent with previous studies (Bokkisa et al., 2022; Yoshimine et al., 1998). The tests support the existence of a unique CSL in e–p' space, as the stress paths approach the previously discussed CSL with minor deviations. In the p'–q space, the triaxial extension critical state stress ratio is estimated as $M = 0.89$, which aligns with the average predictions from the Mohr–Coulomb and Matsuoka–Nakai criteria for extension conditions.

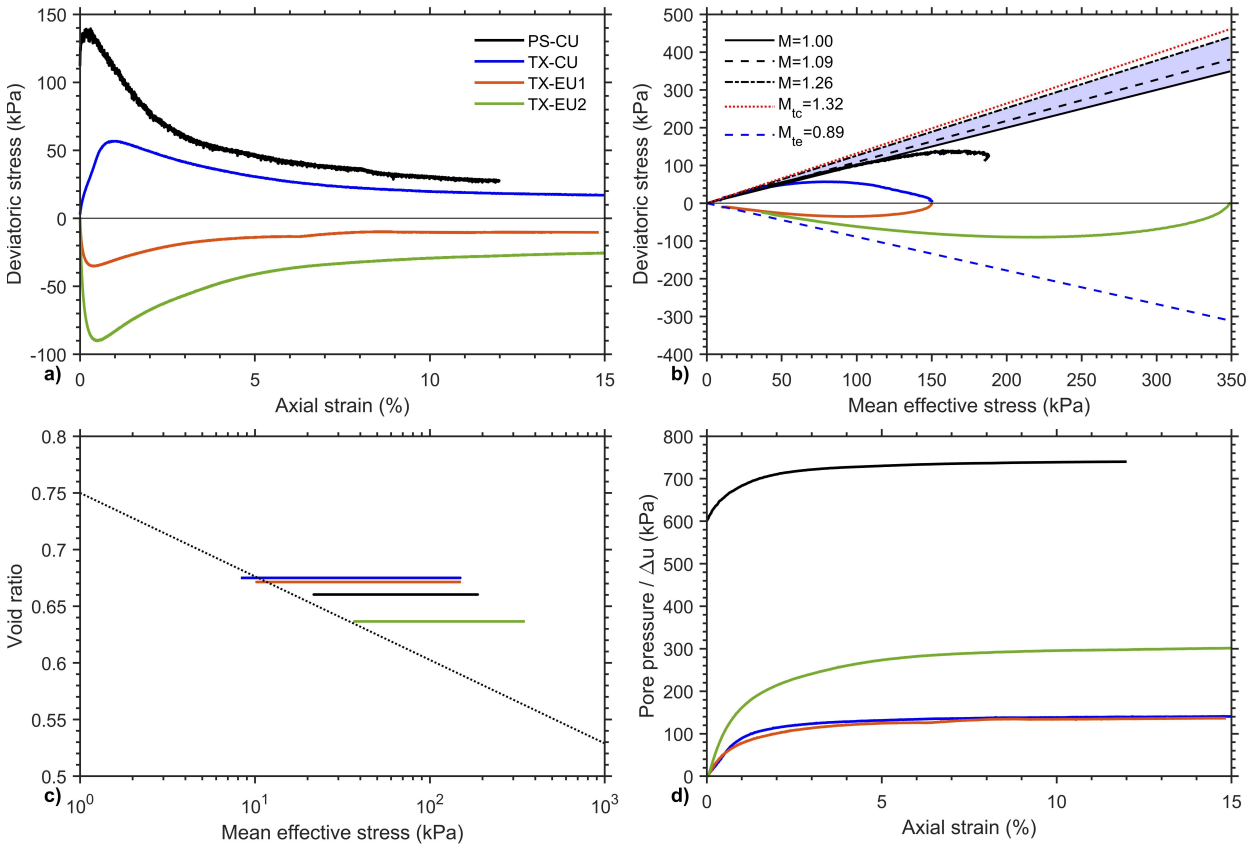

Figure 12: Representative responses for selected undrained triaxial compression (TX4), plane strain compression (PS6) and triaxial extension (TX-EU1, TX-EU2) : (a) q versus axial strain, (b) stress paths in p'–q space with reference critical state lines, (c) Void ratio versus p' showing the critical state line (CSL), and (d) pore pressure evolution with axial strain.

A direct comparison between the present CSD results and those of Wanatowski et al. (2010) is limited by the absence of data near instability in the latter. Their testing system also experienced difficulties in controlling stresses approaching instability. In the present study (Figure 10a), all three principal stresses decrease at different rates prior to instability, after which the intermediate stress increases concurrently with rapid axial (Figure 10e) and volumetric strains (Figure 10b). The pre-instability decrease in intermediate stress is consistent with the absence of axial strain and the simultaneous reduction of major and minor principal stresses. In contrast, Wanatowski et al. (2010) applied stress relief by increasing the back pressure at constant cell pressure. For their loose specimen (IND01; their Figure 8), the measured total intermediate stress increased gradually during stress relief and then dropped sharply at instability, where they reported a loss of test control. Interpretation of the intermediate stress trajectory in their tests is complicated because the measured stress reflects both the rising absolute pressure environment imposed by the back-pressure increase and the soil's tendency to push against the rigid lateral platens as the effective stress state evolves. Decoupling these contributions is not straightforward. In the present study, all total stresses decrease during stress relief, so a measured decrease in intermediate stress followed by a rapid increase near instability more directly reflects the soil response under evolving effective stress.

Finally, the instability stress ratio is examined (Figure 13) for triaxial compression, triaxial CSD, triaxial extension, plane-strain compression, and plane-strain CSD. The instability stress ratio is comparable between triaxial and plane-strain conditions (for both compression and CSD), but lower in triaxial extension. Since the same material was tested, the observations likely reflect the combined influence of loading mode and fabric evolution prior to instability, which are known to be key parameters governing instability onset (Bokkisa et al., 2023, 2022). Similar trends have been reported in numerical simulations by Bokkisa et al. (2022), which also show reduced instability stress ratios in triaxial extension compared

to triaxial compression and plane strain. Further studies examining the influence of loading mode across different materials would help generalize these findings.

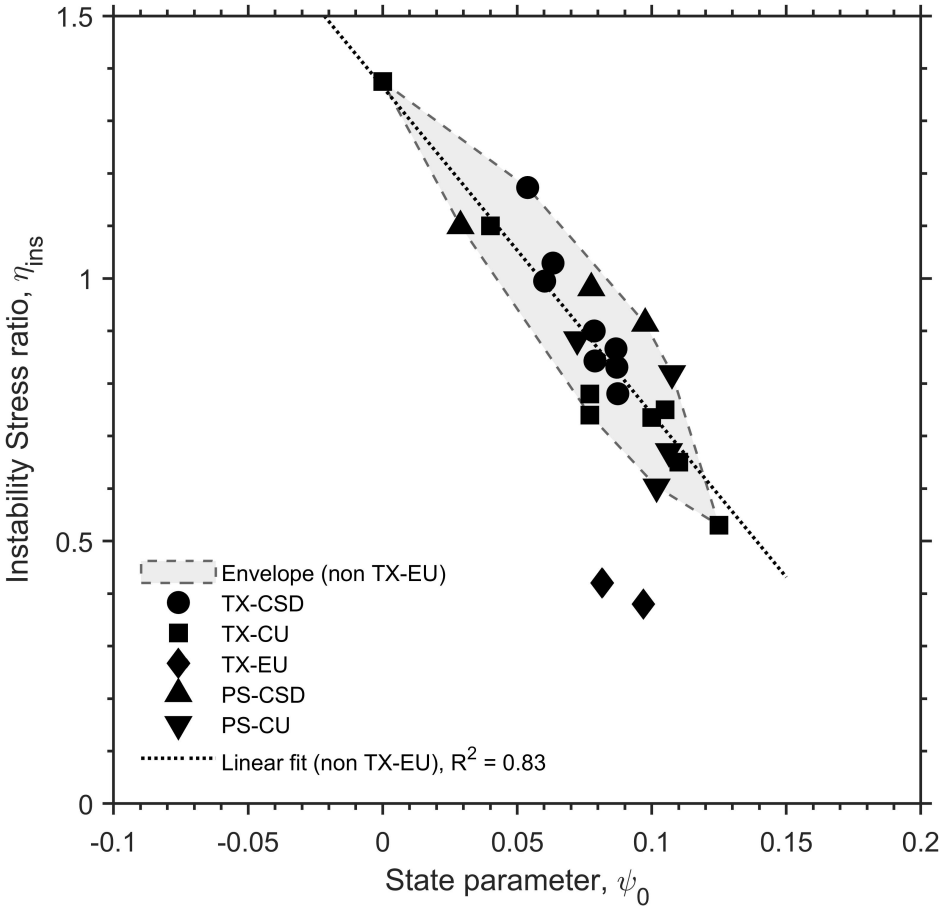

Figure 13: Instability stress ratio, η_{ins}, as a function of initial state parameter, ψ_0, for triaxial (TX) and plane-strain (PS) conditions under different loading paths. The shaded region denotes the envelope excluding triaxial extension results. The dashed line represents the linear fit to non-extension data ($R^2 = 0.83$).

6. Conclusion

This study presents an experimental investigation of mine tailings behavior under plane-strain conditions, including drained and undrained compression and CSD loading, with direct measurement of intermediate stress. Interpretations are conducted under the critical state soil mechanics framework with results providing new insights into the role of loading mode and stress path in governing overall responses and instability onset.

The interpretation of the CSL indicates that, within experimental uncertainty, the CSL in e–p' space is consistent between plane-strain and triaxial conditions for the tested tailing, with independent triaxial extension tests supporting this observation. The inferred CSL parameters ($\Gamma \approx 0.75$, $\lambda \approx 0.032$) are comparable across loading modes, supporting the existence of a unique CSL for this material under evolving intermediate stress conditions. This result is notable, as the only previous study comparing CSLs under triaxial compression and plane strain with direct measurement of intermediate stress (i.e., Wanatowski and Chu (2007)) suggested differences.

In contrast, the critical stress ratio M is influenced by loading mode. Plane-strain tests yield lower M values than triaxial compression, but higher than triaxial extension, consistent with the expected dependence on intermediate stress. The measured responses fall within the bounds defined by Mohr–Coulomb and Matsuoka–Nakai criteria, clustering near their average. The evolution of the intermediate stress ratio b is stress-path dependent, with higher values observed under undrained loading than drained.

Under plane-strain CSD loading, all specimens exhibit Type I instability, characterized by a transition from volumetric expansion to contraction at stress ratios near the lower bound of the expected critical state stress ratio range and at small axial strains. Although the instability stress ratio is comparable under plane-strain and triaxial loading conditions (for both compression and CSD) for the tested material, it is lower under triaxial extension. Furthermore, differences in the evolution of the intermediate principal stress during stress relief distinguish the observed responses, underscoring the role of stress path. The differences on instability stress ratios are consistent with prior numerical studies (Bokkisa and Macedo, 2025; Bokkisa et al., 2022), which indicate that the response is governed by the combined effects of fabric evolution, loading mode, and state. Additional experimental investigations to further explore these mechanisms would be valuable.

Overall, this study presents the first experimental dataset on mine tailings under plane-

strain conditions with direct measurement of intermediate principal stress evolution. The results provide a basis for advancing constitutive models that are predominantly applied under plane-strain assumptions. Continued efforts in this direction are required for improving performance-based TSF assessments, as promoted by the Global Industry Standard on Tailings Management. The findings also establish a foundation for future investigations of plane-strain loading effects across materials with varying mechanical properties.

7. Acknowledgments

This material is based on work supported by the National Science Foundation (NSF) under Grant No. CMMI 2145092. Any opinions, findings, conclusions, or recommendations expressed in this material are those of the author(s) and do not necessarily reflect the views of the NSF.

8. Competing interests

The authors declare there are no competing interests.

9. Data availability

Data generated or analyzed during this study are available from the corresponding author upon reasonable request.

References

Alipour, M., Lashkari, A., 2018. Sand instability under constant shear drained stress path. International Journal of Solids and Structures 150, 66–82. doi:10.1016/j.ijsolstr.2018.06.003.

Alshibli, A.K., Godbold, D.L., Hoffman, K., 2004. The louisiana plane strain apparatus for soil testing. Geotechnical Testing Journal, ASTM 27, 1–10.

Arnold, C., 2025. Liquefaction Response of Mine Tailings and Natural Soils: Novel Experimental Insights and Case Histories. Phd dissertation. Georgia Institute of Technology. Atlanta, GA.

Arroyo, M., Gens, A., 2022. Computational Analyses of Dam I Failure at the Corrego de Feijao Mine in Brumadinho. Technical Report. VALE S.A.

Arthur, J.R.F., Dunstan, T., Enstad, G.G., 1985. Determination of the flow function by means of a cubic plane strain tester. International Journal of Bulk Storage in Silos 1, 7–10.

Becker, L., Fabre, J., Barbosa, M., 2022. Determination of the critical state of a silty sand iron tailings in triaxial extension tests using photographic correction. Canadian Geotechnical Journal 60, 504–520.

Been, K., Conlin, B., Crooks, J., Fitzpatrick, S., Jefferies, M., Rogers, B., Shinde, S., 1987. Back analysis of the nerlerk berm liquefaction slides: Discussion. Canadian Geotechnical Journal 24, 170–179.

Been, K., Jefferies, M., Hachey, J., 1991. The critical state of sands. Géotechnique 41, 365–381.

Bishop, A.W., 1958. The requirements for measuring the coefficient of earth pressure at rest, in: Proceedings of the European Conference on Earth Pressures, Brussels. pp. 1–7.

Bokkisa, S.V., Macedo, J., 2025. Influence of anisotropic consolidation on the instability of loose granular soils under undrained and drained loading. Canadian Geotechnical Journal 62, 1–18. doi:10.1139/cgj-2023-0683.

Bokkisa, S.V., Macedo, J., Petalas, A.L., 2023. Fabric anisotropy effects on static liquefaction under constant shear drained loading. Computers and Geotechnics 163, 105724. doi:10.1016/j.compgeo.2023.105724.

Bokkisa, S.V., Macedo, J., Petalas, A.L., Arson, C., 2022. Assessing static liquefaction triggering considering fabric anisotropy effects under the ACST framework. Computers and Geotechnics 148, 104796. doi:10.1016/j.compgeo.2022.104796.

Campanella, R.G., Vaid, Y.P., 1973. Influence of stress path on the plane-strain behaviour of a sensitive clay, in: Proceedings of the 8th International Conference on Soil Mechanics and Foundation Engineering, Moscow. pp. 85–92.

Cornforth, D.H., 1961. Plane strain failure characteristics of a saturated sand. Ph.D. thesis. University of London.

Cornforth, D.H., 1964. Some experiments on the influence of strain conditions on the strength of sand. Geotechnique 14, 143–167.

Desrues, J., Chambon, R., Mokni, M., Mazerolle, F., 1996. Void ratio evolution inside shear bands in triaxial sand specimens studied by computed tomography. Géotechnique 46, 529–546.

Desrues, J., Lanier, J., Stutz, P., 1985. Localization of the deformation in tests on sand sample. Engineering Fracture Mechanics 21, 909–921.

Desrues, J., Viggiani, G., 2004. Strain localization in sand: an overview of the experimental results obtained in grenoble using stereophotogrammetry. International Journal for Numerical and Analytical Methods in Geomechanics 28, 279–321.

Drescher, A., Vardoulakis, I.G., Han, C., 1990. A biaxial apparatus for testing soils. Geotechnical Testing Journal, ASTM 13, 226–234.

Duncan, J.M., Seed, H.B., 1966. Strength variation along failure surfaces in clay. Journal of the Soil Mechanics and Foundations Division, ASCE 92, 81–104.

Evans, T., 2005. Microscale physical and numerical investigations of shear banding in granular soils. Ph.d. thesis. Georgia Institute of Technology.

Fanni, R., Reid, D., Fourie, A., 2024. Drained and undrained behaviour of a sandy silt gold tailings under general multiaxial conditions. Géotechnique , 1–67.

Finno, R., Rechenmacher, A., 2003. Effects of consolidation history on critical state of sand. Journal of Geotechnical and Geoenvironmental Engineering, ASCE 129, 350–360.

Finno, R.J., Harris, W.W., Mooney, M.A., Viggiani, G., 1997. Shear bands in plane strain compression of loose sand. Géotechnique 47, 149–165.

Finno, R.J., Harris, W.W., Viggiani, G., 1996. Strain localization and undrained steady state of sand. Journal of Geotechnical Engineering, ASCE 122, 462–473.

Fotovvat, A., Sadrekarimi, A., Etezad, M., 2022. Instability of gold mine tailings subjected to undrained and drained unloading stress paths. Géotechnique 74, 174–192. doi:10.1680/jgeot.21.00293.

Frost, J., Evans, T., 2009. Membrane effects in biaxial compression tests. Journal of Geotechnical and Geoenvironmental Engineering 135, 986–991.

Frost, J., Evans, T., Lu, Y., Zhao, X., 2012. Selected observations from 3-d experimental and numerical studies of shear banding in biaxial shear tests, in: GeoCongress 2012: State of the Art and Practice in Geotechnical Engineering, pp. 1116 – 1125.

Frost, J., Yang, C., 2003. Effect of end platens on microstructure evolution in dilatant specimens. Soils and Foundations 43, 1–11.

Hambly, E.C., 1969. A new true triaxial apparatus. Géotechnique 19, 307–309.

Hambly, E.C., 1972. Plane strain behaviour of remoulded normally consolidated kaolin. Géotechnique 22, 301–317.
Hambly, E.C., Roscoe, K.H., 1969. Observations and predictions of stresses and strains during plane-strain of "wet" clays, in: Proceedings of the 7th International Conference on Soil Mechanics and Foundation Engineering, Mexico. pp. 173–181.
Hill, R., 1958. A general theory of uniqueness and stability in elastic-plastic solids. Journal of the Mechanics and Physics of Solids 6, 236–249. doi:10.1016/0022-5096(58)90029-2.
Jefferies, M., Been, K., 2016. Soil liquefaction: a critical state approach, 2nd ed. CRC Press.
Jefferies, M., Shuttle, D., 2002. Dilatancy in general cambridge-type models. Géotechnique 52, 625–638.
Ladd, R., 1978. Preparing test specimens using undercompaction. Geotechnical Testing Journal 1 (1), 1–8. URL: https://doi.org/10.1520/GTJ10364J.
Lee, K.L., 1970. Comparison of plane strain and triaxial tests on sand. Journal of the Soil Mechanics and Foundations Division, ASCE 96, 901–923.
Leussink, H., Wittke, W., 1964. Difference in triaxial and plane strain shear strength, in: Laboratory Shear Testing of Soils. ASTM STP 361, pp. 77–89.
Macedo, J., Vergaray, L., 2021. Properties of mine tailings for static liquefaction assessment. Canadian Geotechnical Journal 59, 667–687.
Morgenstern, N.R., Jefferies, M., Zyl, D., Wates, J., 2019. Independent Technical Review Board: Report on NTSF Embankment Failure. Technical Report. Ashurst Australia.
Morgenstern, N.R., Vick, S.G., Viotti, C.B., Watts, B.D., 2016. Fundao Tailings Dam Review Panel: Report on the Immediate Causes of the Failure of the Fundao Dam. Technical Report. Cleary Gottlieb Steen and Hamilton LLP. New York. Available at: http://fundaoinvestigation.com/the-panel-report/.
Olson, S., Stark, T., Walton, W., Castro, G., 2000. 1907 static liquefaction flow failure of the north dike of wachusett dam. Journal of Geotechnical and Geoenvironmental Engineering 126 (12).
Reid, D., Fanni, R., Fourie, A., 2024. A SHANSEP approach to quantifying the behaviour of clayey soils on a constant shear drained stress path. Canadian Geotechnical Journal , 1–24doi:10.1139/cgj-2022-0473.
Reid, D., Fourie, A., Ayala, J., Dickinson, S., Ochoa-Cornejo, F., Fanni, R., Garfias, A., Da Fonseca, A., Ghafghazi, M., Ovalle, C., Riemer, M., Rismanchian, A., Suazo, G., 2020. Results of a critical state line testing round robin programme. Géotechnique 71 (7), 616–630. URL: http://dx.doi.org/10.1680/jgeot.19.p.373.
Riemer, M., Seed, R., 1997. Factors affecting apparent position of steady-state line. Journal of Geotechnical and Geoenvironmental Engineering, ASCE 123, 281–288.
Rietveld, H., 1969. A profile refinement method for nuclear and magnetic structures. Journal of Applied Crystallography , 65–71.
Riveros, G.A., Sadrekarimi, A., 2021. Static liquefaction behaviour of gold mine tailings. Canadian Geotechnical Journal 58, 889–901. doi:10.1139/cgj-2020-0209.
Roscoe, K.H., Schofield, A.N., Wroth, C.P., 1958. On the yielding of soils. Géotechnique 8, 22–53.
Rowe, P., 1969. The relation between the shear strength of sands in triaxial compression, plane strain, and direct shear. Géotechnique 19, 75–86.
Salvatore, E., Modoni, G., Andò, E., Albano, M., Viggiani, G., 2017. Determination of the critical state of granular materials with triaxial tests. Soils and Foundations 57, 733–744.
Schnaid, F., Bedin, J., Viana da Fonseca, A., de Moura Costa Filho, L., 2013. Stiffness and strength governing the static liquefaction of tailings. Journal of Geotechnical and Geoenvironmental Engineering 139, 2136–2144.
Schofield, A., Wroth, P., 1968. Critical State Soil Mechanics. 1 ed., McGraw-Hill.
Sladen, J., Handford, G., 1987. A potential systematic error in laboratory testing of very loose sands. Canadian Geotechnical Journal 24, 462–466.
Tatsuoka, F., Sakamoto, M., Kawamura, T., Fukushima, S., 1986. Strength and deformation characteristics of sand in plane strain compression at extremely low pressures. Soils and Foundations 26, 65–84.
Tatsuoka, F., Sato, T., Park, C.S., Kim, Y.S., Mukabi, J.N., Kohata, Y., 1994. Measuring of elastic properties of geomaterials in laboratory compression tests. Geotechnical Testing Journal, ASTM 17, 80–94.

Topolnicki, M., Gudehus, G., Mazurkiewicz, B.K., 1990. Observed stress-strain behaviour of remoulded saturated clay under plane-strain conditions. Géotechnique 42, 155–187.
Torres-Cruz, L.A., Santamarina, J.C., 2019. The critical state line of nonplastic tailings. Canadian Geotechnical Journal 57, 1508–1517. doi:10.1139/cgj-2019-0019.
Velten, R.Z., Ulsen, C., Rodrigues da Costa, J.P., Alves Lima, C.A., Mafessoli, M., de Azambuja Carvalho, J.V., Consoli, N.C., 2025. Role of mineralogy on the undrained monotonic simple shear response of compacted filtered copper tailings. Soils and Foundations 65, 101636. doi:10.1016/j.sandf.2025.101636.
Verdugo, R., Ishihara, K., 1996. The steady state of sandy soils. Soils and Foundations 36, 81–91.
Vergaray, L., Macedo, J., 2024. Mechanical response of mine tailings under constant shear drained loading. Journal of Geotechnical and Geoenvironmental Engineering 150.
Wagner, A., de Sousa Silva, J., de Azambuja Carvalho, J., Rissoli, A., Cacciari, P., Chaves, H., Scheuermann Filho, H., Consoli, N., 2023. Mechanical behavior of iron ore tailings under standard compression and extension triaxial stress paths. Journal of Rock Mechanics and Geotechnical Engineering 15, 1883–1894.
Wanatowski, D., 2005. Strain softening and instability of sand under plane-strain conditions. Doctor of engineering thesis. Nanyang Technological University. Singapore.
Wanatowski, D., Chu, J., 2006. Stress-strain behavior of a granular fill measured by a new plane-strain apparatus. Geotechnical Testing Journal, ASTM 29, 149–157.
Wanatowski, D., Chu, J., 2007. Static liquefaction of sand in plane strain. Canadian Geotechnical Journal 44, 299–313. doi:10.1139/t06-078.
Wanatowski, D., Chu, J., 2012. Factors affecting pre-failure instability of sand under plane-strain conditions. Geotechnique 62, 121–135.
Wanatowski, D., Chu, J., Lo, R., 2008. Strain-softening behaviour of sand in strain path testing under plane-strain conditions. Acta Geotechnica , 99–114doi:10.1007/s11440-008-0064-1.
Wanatowski, D., Chu, J., Loke, W., 2010. Drained instability of sand in plane strain. Canadian Geotechnical Journal 47, 400–412.
Wang, L., Chu, J., Wu, S., 2024. Mechanical behavior of cemented sand under plane strain condition. International Journal of Geomechanics 24. doi:10.1061/IJGNAI.GMENG-10368.
Wu, Y., Hyodo, M., Cui, J., 2020. On the critical state characteristics of methane hydrate-bearing sediments. Marine and Petroleum Geology 116, 104342. URL: https://www.sciencedirect.com/science/article/pii/S0264817220301252, doi:10.1016/j.marpetgeo.2020.104342.
Yasin, S.J.M., Umetsu, K., Tatsuoka, F., Arthur, J.R.F., Dunstan, T., 1999. Plane-strain strength and deformation of sands affected by batch variations and different apparatus types. Geotechnical Testing Journal, ASTM 22, 80–100.
Yoshimine, M., Ishihara, K., Vargas, W., 1998. Effects of principal stress direction and intermediate principal stress on undrained shear behavior of sand. Soils and Foundations 38, 179–188.

Appendix A

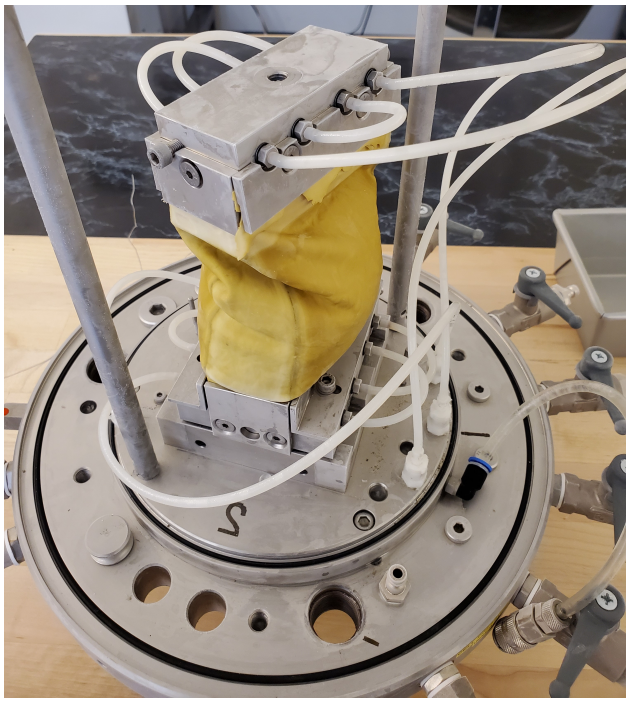

Figure A.1: Fully frozen plane-strain specimen after removal from freezer.

Table A.1: Plane-strain compression, CSD, and triaxial extension tests conducted in this study with complementary triaxial compression tests

Test	Loading Type	Drainage Condition	p'_0 (kPa)	e_0
PS1	Plane-strain compression	Undrained	114	0.721
PS2	Plane-strain compression	Undrained	100	0.718
PS3	Plane-strain compression	Undrained	91	0.713
PS4	Plane-strain compression	Drained	57	0.707
PS5	Plane-strain compression	Drained	85	0.681
PS6	Plane-strain compression	Undrained	187	0.660
PS7	Plane-strain compression	Drained	100	0.661
PS8	Plane-strain compression	Drained	100	0.651
PS9	Plane-strain compression	Drained	209	0.618
PS10	Plane-strain CSD	Drained	106	0.700
PS11	Plane-strain CSD	Drained	252	0.660
PS12	Plane-strain CSD	Drained	317	0.600
TX18-EU1	Triaxial Extension	Undrained	150	0.670
TX19-EU2	Triaxial Extension	Undrained	346	0.640
TX1	Triaxial compression	Undrained	50	0.738
TX2	Triaxial compression	Undrained	40	0.730
TX3	Triaxial compression	Undrained	148	0.688
TX4	Triaxial compression	Undrained	150	0.675
TX5	Triaxial compression	Undrained	150	0.650
TX6	Triaxial compression	Drained	249	0.640
TX7	Triaxial compression	Drained	100	0.638
TX8	Triaxial compression	Drained	249	0.634
TX9	Triaxial compression	Drained	350	0.627
TX10	Triaxial compression	Undrained	348	0.622
TX11	Triaxial compression	Undrained	501	0.610
TX12	Triaxial compression	Undrained	25	0.600
TX13	Triaxial compression	Drained	251	0.583
TX14	Triaxial compression	Drained	99	0.561
TX15	Triaxial compression	Undrained	65	0.560
TX16	Triaxial compression	Undrained	332	0.530
TX17	Triaxial CSD	Drained	353	0.63